Distinct intermediate states in the isostructural *R*-3*m* phase of the topological insulator Bi_2Se_3 at high pressure

Xinguo Hong [1,*] Matt Newville,[2] Yang Ding,[1] Tetsuo Irifune,[3] Genda Gu,[4] and Ho-Kwang Mao[1,5]

[1]*Center for High Pressure Science and Technology Advanced Research, Beijing 100094, People's Republic of China*
[2]*Consortium for Advanced Radiation Sources, University of Chicago, Chicago, Illinois 60637, USA*
[3]*Geodynamics Research Center, Ehime University, Matsuyama 790-8577, Japan*
[4]*Condensed Matter Physics and Materials Science Department, Brookhaven National Laboratory, Upton, New York 11973, USA*
[5]*Geophysical Laboratory, Carnegie Institution of Washington, Washington, DC 20015, USA*

(Received 29 January 2020; revised manuscript received 26 May 2020; accepted 27 May 2020; published 11 June 2020)

The electronic state of layered three-dimensional topological insulators at high pressure is a compelling but a puzzling hot topic. The open question is the structural origins for the pressure-induced novel physics of electronic topological transition (ETT), topological superconductivity, and Majorana fermions in the same isostructural *R*-3*m* phase. Here, we report a combined investigation on the local structure and bulk electronic state of topological insulator Bi_2Se_3 using x-ray diffraction, high quality x-ray absorption fine-structure spectroscopies both at the Bi L_3 edge and at the Se *K* edge, and first-principles theoretical calculations. We have found three pressure-induced distinct intermediate states in the isostructural rhombohedral phase of Bi_2Se_3. The bulk electronic structure of the *R*-3*m* phase was calculated based on the experimental structure. The corresponding distinct electronic states provide the origins of ETT at ~3 GPa and the metallization at 7–9.5 GPa in the *R*-3*m* phase of Bi_2Se_3. Our results demonstrate that the local structure plays a critical role in the electronic states of topological insulator Bi_2Se_3.

DOI: 10.1103/PhysRevB.101.214107

I. INTRODUCTION

The three-dimensional (3D) topological insulators (TIs) (Bi_2Se_3, Bi_2Te_3, and Sb_2Te_3) have been extensively studied in the past decade [1–4]. At high pressure, the layered tetradymite structure (*R*-3*m*, No. 166) shows amazing novel physics, such as a common electronic topological transition (ETT) at 3–5 GPa [5] and topological superconductivities [6,7]. The ETT is an isostructural phase transition (IPT) but can lead to considerable changes and anomalies in the mechanical, vibrational, electrical, thermodynamic, and transport properties [8–10]. The topological superconductors have superconductivity in the bulk and a gapless surface state protected by time-reverse symmetry [11] where the long-sought Majorana fermion is predicted [12].

There are still several puzzling questions regarding the novel physics in this rhombohedral *R*-3*m* phase of TI materials, e.g., the underlying mechanism of ETT [4,13,14], interplay between bulk and surface states [15,16], high-pressure phase sequence [4,17–19], and topological superconductors [20]. The superconductivity was discovered in the *R*-3*m* phase of the topological insulators Bi_2Te_3 [6,21] and Sb_2Te_3 [7] but not for Bi_2Se_3 [22] somehow.

The understanding of these novel physics depends critically on the knowledge of the crystal structure, electronic band structure, bulk and surface electronic states, carrier concentration, and spin-orbit interactions [11]. To solve the mystery of the *R*-3*m* phase, it is, therefore, of great importance to study the local structure at high pressure. So far, x-ray diffraction (XRD) has played a dominant role in the high-pressure structure determination [23], whereas x-ray absorption fine-structure spectroscopy (XAFS) for local structural studies in the layered TIs are very scarce [24]. XAFS is a well-established technique to probe the local atomic and electronic structures around the absorber atoms. Among the 3D TIs (Bi_2Se_3, Bi_2Te_3, and Sb_2Te_3), the local structure of Bi_2Se_3 is very interesting because both local structures of Bi and Se atoms can be directly measured by XAFS techniques. However, high-pressure XAFS suffers from the Bragg reflections of single-crystal diamond anvils, and its application has been severely limited [25]. Recently, the nanopolycrystalline diamond (NPD) anvil has proven to be promising for glitch-free XAFS spectra [26,27].

As a clean and effective tool, high pressure has been widely applied to tune the interatomic distances, crystal structures, electronic and topological states, and physical properties without introducing the disorders inherent to chemical doping [20]. In this paper, we report a combined investigation of high-pressure XAFS (HP-XAFS) experiments using NPD anvils, XRD, and first-principles theoretical calculations on the topological insulator Bi_2Se_3 up to 15 GPa, covering the ETT at 3–5 GPa, metallization at 9.7 GPa, and the onset of superconductivity at 11 GPa.

*Corresponding author: xinguo.hong@hpstar.ac.cn; xinguo.hong@gmail.com

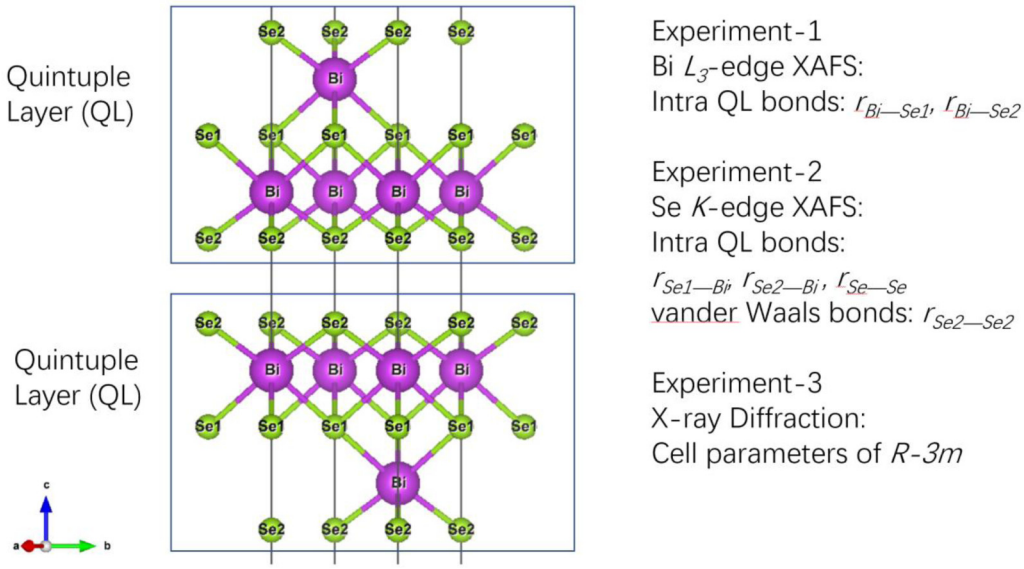

FIG. 1. Crystal structure of Bi_2Se_3. The rhombohedral R-3m crystal structure of Bi_2Se_3 consists of hexagonal planes of Bi and Se stacked on top of each other along the c direction forming a QL with Se2-Bi-Se1-Bi-Se2 where Se1 is on the QL central plane whereas Se2 is on the QL surface. The structure of QLs under high pressure is probed by three complementary experiments.

II. EXPERIMENT

A. Crystal growth and preparation

The Bi_2Se_3 single crystals in this paper were grown by a unidirectional solidification method with slowly cooling down. The samples were loaded into NPD cells for high-pressure XAFS and XRD experiments.

B. High-pressure XAFS

A Princeton-manufactured large-opening symmetrical diamond-anvil cell (DAC) was employed with a pair of 600-μm culet NPD anvils. A rectangle foil of rhenium was preindented down to a thickness of 40 μm. A gasket hole of 220 μm was drilled at the indention center in the foil. XAFS experiments were carried out at both the Se K edge and the Bi L_3 edge of Bi_2Se_3 sample in the transmission mode at the GeoSoilEnviroCARS undulator beamline 13-ID-E, Advanced Photon Source (APS), Argonne National Laboratory. The x-ray beam size was focused down to a square spot of 1- to 2-μm size using Kirkpatrick-Baez mirrors that were spatially stable over the entire energy scan. XAFS spectra were collected with 5-eV steps before the main edge, 0.2-eV steps from -10 to 25 eV across the Se K edge (12 658 eV) and Bi L_3 edge (13 419 eV) and 0.05-Å^{-1} steps in k space to 14 Å^{-1} above the main edges. XAFS data analysis were proceeded using the ATHENA and ARTEMIS programs [28] implemented IFEFFIT package [29].

C. High-pressure synchrotron angular dispersive XRD

In situ angular dispersive XRD were collected using a PerkinElmer flat panel detector (XRD 1261). The x-ray energy of x-ray diffraction was fixed at 18 keV. This large-area detector facilitates data collection to cover a wide Q range. The sample-detector distance and detector orientation were calibrated using a CeO_2 standard. Pressure was measured both before and after each XAFS/XRD measurement, and the pressure difference was typically 0.25 GPa or less. The two-dimensional image plate patterns were integrated to the one-dimensional patterns by using the FIT2D software [30] with a masked diffraction ring of NPD anvils prior to the integration. The resulting diffraction patterns were fitted via Rietveld refinement through the JANA2006 package [31].

D. Density functional calculation

Density functional theory (DFT) calculations were performed using the Perdew-Zunger-type [32] generalized gradient approximation (GGA) [33] implemented in the QUANTUM ESPRESSO code [34]. Full relativistic pseudopotentials (Bi.rel-pz-dn-rrkjus_psl.1.0.0.UPF and Se.rel-pz-n-rrkjus_psl.0.2.UPF) were used in the calculation of the bulk electronic structure of Bi_2Se_3. Spin-orbit coupling (SOC) has been included. The calculations were performed with a plane-wave cutoff of 50 Ry on an $8 \times 8 \times 8$ k-point mesh. The lattice parameters were determined by XRD experiment, but the Wyckoff positions of atoms were calculated from the Bi-Se bond length obtained by the HP-XAFS experiment. At each pressure step, we calculated band structures along the high-symmetry lines (Γ-Z-F-Γ-L) in the Brillouin zone of the R-3m structure. The values of the band gap were computed with and without XAFS optimization on the Wyckoff positions of atoms for comparison.

Perdew-Burke-Ernzerhof pseudopotentials [35] were used for non-SOC band-gap calculation for comparison.

III. RESULTS AND DISCUSSION

At ambient pressure, the Bi_2Se_3 crystal contains five atomic planes with Se2-Bi-Se1-Bi-Se2 stacking in a quintuple layer (QL) along the c axis (Fig. 1). The Bi sites locate inside the QL, whereas there are two inequivalent Se atoms (Se1 and

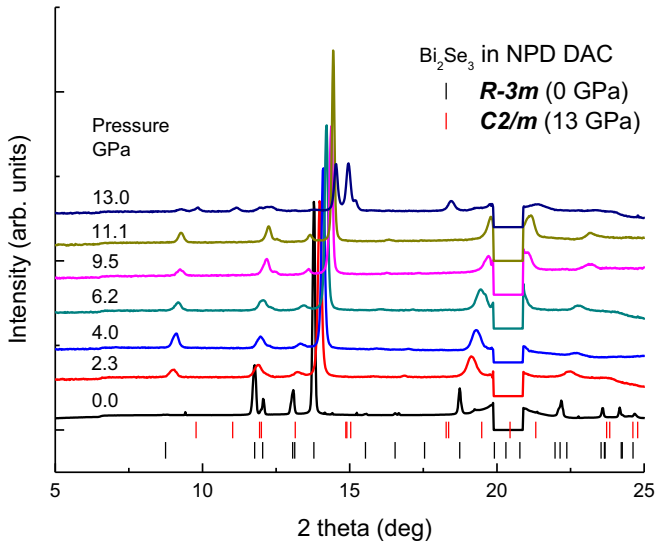

FIG. 2. The selected angle-dispersive XRD patterns of Bi_2Se_3 with NPD anvils under various pressures at room temperature from ambient pressure up to 13 GPa. The vertical bars are the expected diffraction lines of R-3m and $C2/m$ phases at 0 and 13 GPa, respectively.

Se2) occupying the central and the outermost planes of a QL, respectively. The Se1 site on the central plane of the QL is the inversion center of the R-3m structure. Bonds inside the QL are of ionic-covalent type, whereas the outermost interlayer Se2-Se2 bonds between adjacent QLs are linked by weak van der Waals forces.

We designed three complementary experiments to address the pressure-induced structural changes as shown in Fig. 1. The Bi L_3-edge XAFS experiment is aimed to measure the ionic-covalent bonds inside the QLs ($r_{\text{Bi-Se1}}$,$r_{\text{Bi-Se2}}$). The Se K-edge XAFS is to probe both the intralayer QL bonds ($r_{\text{Se1-Bi}}$,$r_{\text{Se2-Bi}}$, $r_{\text{Se-Se1/Se2}}$) and the interlayer vander Waals bonds between QLs ($r_{\text{Se2-Se2}}$). Lattice parameters of Bi_2Se_3 were determined by *in situ* XRD experiments.

Figure 2 shows the selected angle-dispersive XRD patterns of Bi_2Se_3 loaded into NPD anvils under various pressures from ambient pressure up to 13 GPa. The black and red vertical bars denote the expected diffraction lines of R-3m and $C2/m$ phases, respectively. The pressure-induced structural phase transitions of Bi_2Se_3 have been studied extensively [4,17–19,22,36]. It is clear that Bi_2Se_3 undergoes a phase-transition sequence of R-3m $\rightarrow$ $C2/m$ $\rightarrow$ $C2/c$ $\rightarrow$ $I4/mmm$ structures at high pressure despite some uncertainties in the phase boundary [17,18,22,36]. The reported pressure of R-3m $\rightarrow$ $C2/m$ phase transition ranges from 9.1 to 11.4 GPa [4,17–19,22,36]. As shown in Fig. 2, the R-3m phase of Bi_2Se_3 is totally stable up to 11 GPa without emergence of an appreciable amount of the $C2/m$ phase. This agrees well with the previous work [18] by using Bi_2Se_3 single crystals with the same growth method where the R-3m to $C2/m$ phase transition is reported to take place at pressures above

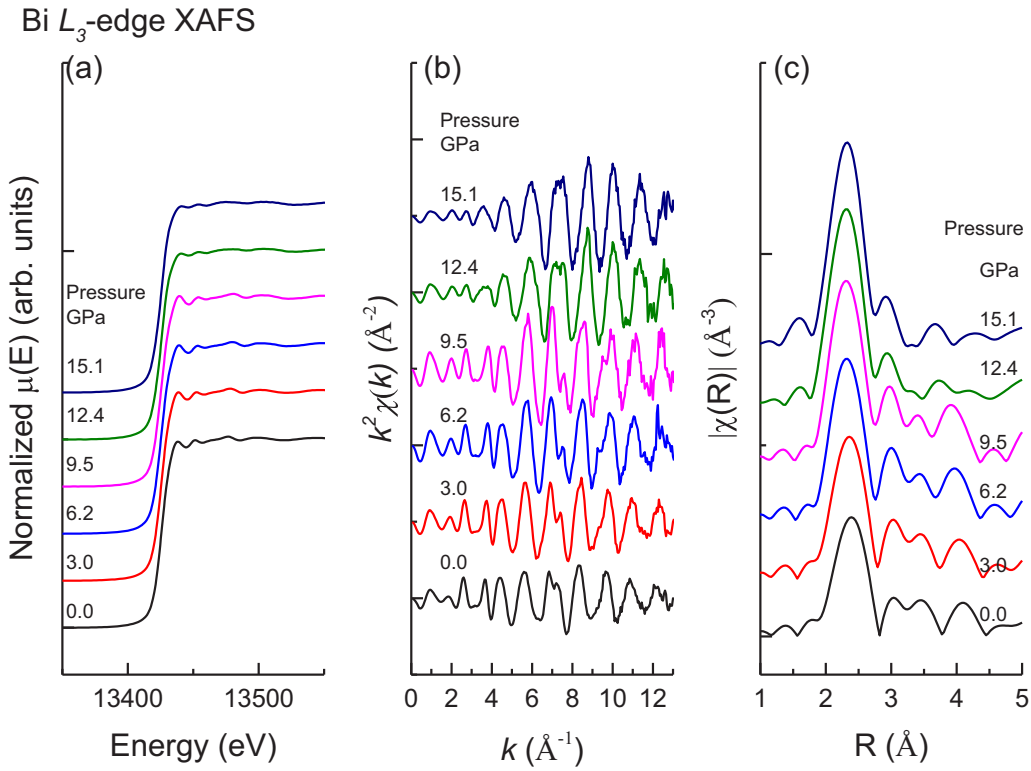

FIG. 3. Selected Bi L_3-edge XAFS of Bi_2Se_3 as a function of pressure by high-pressure XAFS using NPD anvils. (a) Normalized x-ray absorption $\mu(E)$ as the x-ray appearance near-edge structure (XANES) region. (b) k^2- weighted XAFS spectra $k^2\chi(k)$ with a noticeable change in the XAFS oscillation profile (6−11 Å^{-1}) as pressure increases. (c) XAFS Fourier transform $|\chi(R)|$ obtained in the range from 2.5 to 12.5 Å^{-1} with a Hanning window. Note the merging of two peaks (2.8–3.5 Å) above 12.4 GPa.

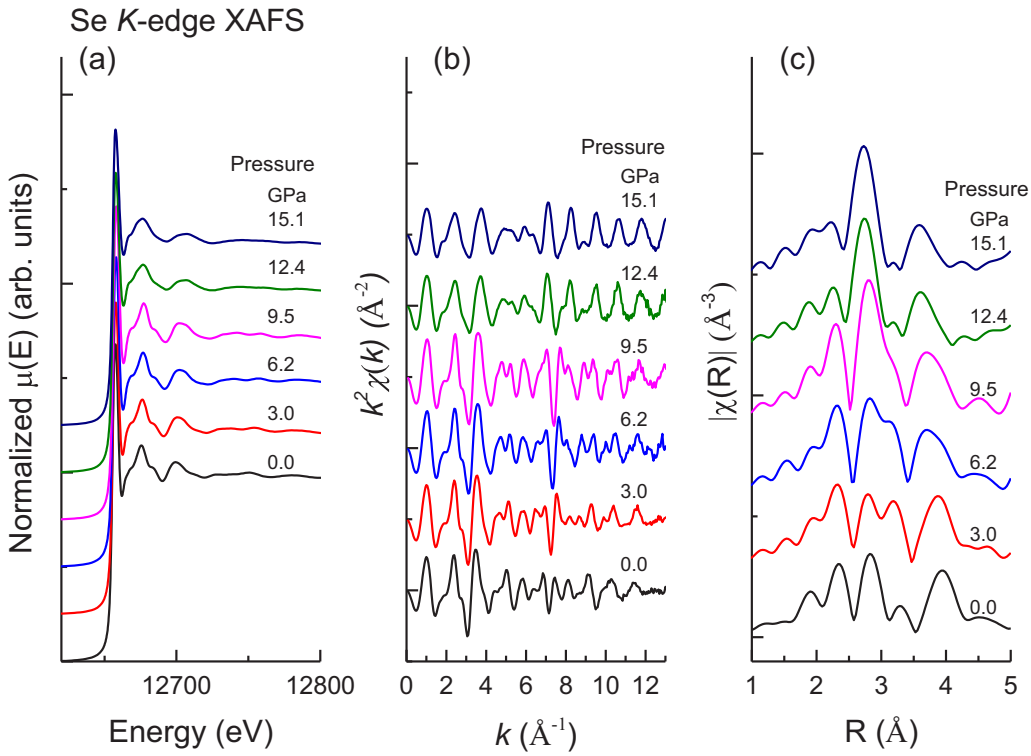

FIG. 4. Selected Se K-edge XAFS of Bi_2Se_3 as a function of pressure by high-pressure XAFS using NPD anvils. (a) Normalized x-ray absorption $\mu(E)$ in the XANES region. (b) k^2-weighted XAFS spectra $k^2\chi(k)$ with considerable pressure-induced change in the XAFS oscillation profile ($3-11$ Å^{-1}). (c) XAFS Fourier transform $|\chi(R)|$ in the range from 2.5 to 12.5 Å^{-1} with a Hanning window. Note the side peak (3.1–3.5 Å), enhancing (<3 GPa), decreasing (4.2–10.4 GPa), and merging (>12.4 GPa).

11.4 GPa. The lattice parameter of R-3m at 13 GPa (Fig. 2) can be deduced from the mixed diffraction pattern of R-3m and $C2/m$ phases.

Figure 3 shows the selected XAFS data of Bi_2Se_3 at the Bi L_3 edge as a function of pressure. Both the XANES [Fig. 3(a)] and the extended x-ray-absorption fine-structure [Fig. 3(b)] regions are free of DAC imposed glitches. The k^2-weighted XAFS spectra, $k^2\chi(k)$, are of high quality with a good signal to noise ratio out to 13 Å^{-1}. This confirms that the DAC with a NPD anvil is well suited to acquire high-quality XAFS data at high pressure [26,27] in contrast to the single-crystalline anvil where the residual glitches may cause deformation in XAFS spectra and result in considerable uncertainties in the further structural modeling [25].

There is a noticeable enhancement in the XAFS oscillation ($6-11$ Å^{-1}) as pressure increases [Fig. 3(b)]. The atomic distribution in real-space (no phase correction) $|\chi(R)|$, was obtained by Fourier transform of $k^2\chi(k)$ in the range from 2.5 to 12.5 Å^{-1} with a Hanning window [Fig. 3(c)]. The two peaks at 2.8—3.5 Å merges at pressures above 12.4 GPa, being a sign of phase transition from rhombohedral (R-3m) to the bcclike ($C2/m$) structure [4].

The selected Se K-edge XAFS spectra of Bi_2Se_3 are shown in Fig. 4 as a function of pressure. All the XAFS data, i.e., the normalized $\mu(E)$ [Fig. 4(a)], k^2-weighted XAFS spectra, $k^2\chi(k)$ [Fig. 4(b)], and the Fourier transform modulus $|\chi(R)|$ [Fig. 4(c)] are of good quality free of DAC imposed glitches out to 13 Å^{-1}, making it feasible for further structural modeling with multiple coordination shells into the medium-range order. The XAFS profiles [Figs. 4(b) and 4(c)] exhibit more structural features than that of Bi L_3-edge XAFS [Figs. 3(b) and 3(c)]. Pressure-induced change in the $k^2\chi(k)$ profile is clear at $3-11$ Å^{-1}. The XAFS modulus of $|\chi(R)|$ was Fourier transformed in the range of $2.5-12.5$ Å^{-1} using a Hanning window. The side peak at 3.1–3.5 Å (no phase correction) shows a notable enhancement and finally merged with the main peak (>12.4 GPa). These observations indicate that there are profound changes in the local structures of both Bi and Se sites at high pressure during the ETT transition (~3 GPa) and the R-3m to $C2/m$ phase transition above 11 GPa.

Figure 5(a) shows typical Rietveld refinements for the lattice parameters of the R-3m phase using JANA2006 software [31]. We do not refine the atomic position at this stage because of: (1) XAFS is much more sensitive for subtle change in bond length or the relative atomic distance; (2) it is hard for a conventional powder XRD experiment to provide precise atomic position unlike the case of single-crystal diffraction, which requires a full set of Bragg peaks with accurate diffraction intensities. The powder diffraction intensity depends on the crystal orientations, grain size, texture, etc., which is difficult to control under high pressure.

Figures 5(b) and 5(c) show the experimental XAFS data of Bi_2Se_3 measured at the Bi L_3 edge and the Se K edge, respectively, at ambient pressure (black line) with fits by the theoretical FEFF calculation (red line) based on the R-3m structure using ARTEMIS [28]. The difference between the experimental XAFS data and the XRD structural model suggests

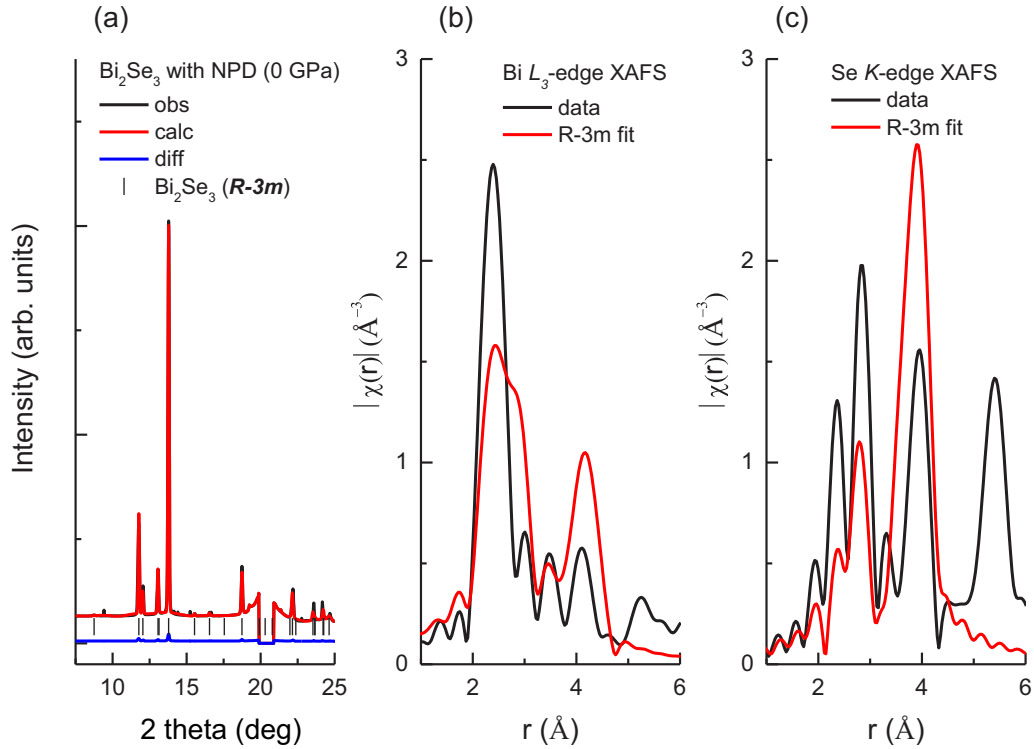

FIG. 5. (a) Typical Rietveld refinements of the diffraction patterns of Bi_2Se_3 loaded in a NPD cell using JANA2006 software [31]. (b) Bi L_3-edge XAFS of Bi_2Se_3 data $|\chi(R)|$ at ambient pressure (black line) together with the theoretical data from the FEFF calculation (red line). (c) Se K-edge XAFS of Bi_2Se_3 data $|\chi(R)|$ at ambient pressure (black line) together with the theoretical data from the FEFF calculation (red line).

that there is an appreciable deviation of the local structure at both the Bi site and the Se site from the long-range periodic structure. It would be particularly important to characterize and explore the electronic structure of Bi_2Se_3 if we can combine both experimental results of XAFS and XRD into the first-principles theoretical calculation.

Figure 6 shows the obtained local structure of Bi_2Se_3 QLs at high pressure. For the Bi L_3-edge XAFS data [Fig. 3(c)], the Bi atoms have a well-defined first coordination shell in contrast to that of Se sites by Se K-edge XAFS [Fig. 4(c)]. We use the well-established model-independent first-shell fitting to fit the Bi L_3-edge XAFS data (2 to 3 $Å^{-1}$). Two FEFF single paths of Bi-Se1 (central QL bond, Fig. 1) and Bi-Se2 (outmost QL bond, Fig. 1) in the first coordination shell of the R-3m structure were used. Figures 6(a) and 6(b) show the obtained Bi-Se bond and Debye-Waller (DW) factor σ^2, respectively, as a function of pressure.

There is a slight kink in the pressure dependence of the Bi-Se2 bond upon the ETT at ∼3 GPa. At above 11 GPa, a substantial reduction in the Bi-Se2 bond occurs, whereas the central Bi-Se1 bond changes slightly with increasing pressure [Fig. 6(a)]. For the DW factor [Fig. 6(b)], there is a disorder-to-order transition up to 11 GPa both for Bi-Se1 and for Bi-Se2 bonds. This disorder-to-order transition is reported here. This pressure-induced ordering inside QLs also rules out the speculation that the disorder may play a dominant role in the anomalies of resistivity and thermopower during the ETT or IPT [37]. Above 11 GPa, other opposite disorder-driven transition appears. It is remarkable that much larger disordering occurs for the Bi-Se1 bonds than that of the Bi-Se2 bonds, i.e., the disordering largely happens on the central plane of QLs above 11 GPa where the onset is of topological superconductivity [22]. This suggests that disordering on the central plane of QL may play an important role in the emergence of topological superconductivity in Bi_2Se_3.

It is known that the first-shell fitting suffers from large errors [Figs. 6(a) and 6(b)] because of limited data employed in the fitting. Figure 6(c) shows a typical fit of multiple coordination shells to the Se K-edge XAFS data of Bi_2Se_3 at 8.6 GPa (full circles) based on the full set of single scattering paths of the R-3m structure within a cluster of 4.5 Å. This modeling in the medium-range order provides more details of the local structure in the QLs: the intralayer ionic-covalent bonds of Se2-Bi, Se1-Bi, and Se-Se bonds inside the QL and the interlayer van der Waals bond Se2-Se2 between QLs. To keep the integrity of the R-3m cluster, we made no change in the path degeneracies and relative amplitudes. The evolution of the four coordination distances in the QLs is shown in Fig. 6(d).

All two kinds of intralayer ionic-covalent bonds (Se2-Bi and Se1-Bi) inside the QL and the interlayer van der Waals bond (Se2-Se2) between QLs show a change in the linear slope at ∼3 GPa where the ETT occurs. Table I lists the linear fitting parameters around this ETT transition. It can be seen that the Se2-Bi bond has the smallest change in linear slope, i.e., little relevance to the ETT, whereas there are much larger changes for the central Se1-Bi bond and interlayer distances, Se2-Se2, during ETT transition. This indicates that both the

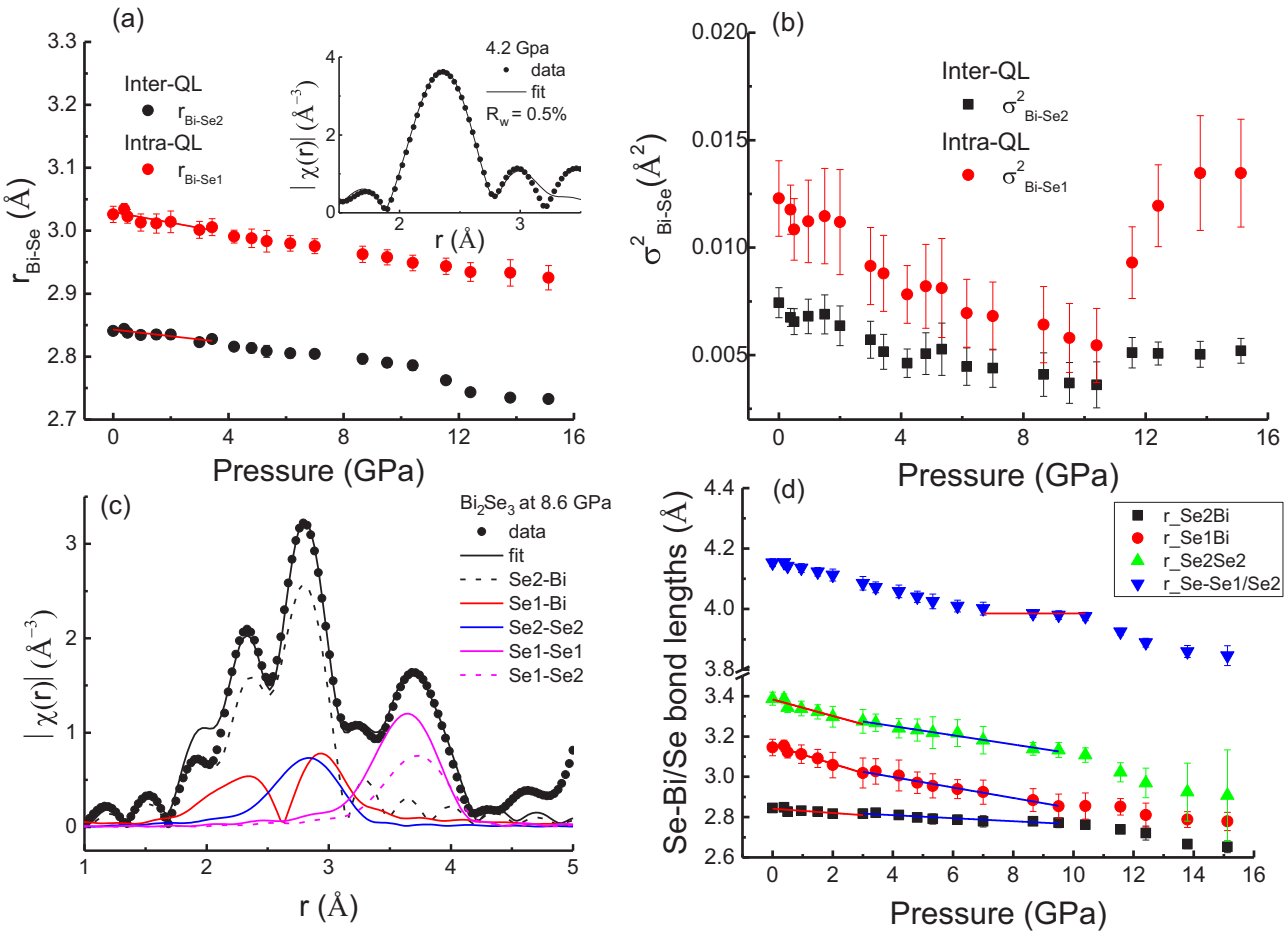

FIG. 6. Upper panel: Bi L_3-edge XAFS of Bi_2Se_3. (a) Evolution of the nearest Bi-Se1 and Bi-Se2 distances of Bi_2Se_3 QLs as a function of pressure. (b) Pressure dependence of the DW factor σ^2. Lower panel: Se K-edge XAFS of Bi_2Se_3. (c) Structural modeling of XAFS data $|\chi(R)|$ for Bi_2Se_3 at 8.6 GPa (full circles) using the paths of the R-3m structure within 4.5 Å^{-1}. (d) Evolution of the Se-Bi and Se-Se bonds of the Bi_2Se_3 QL at high pressure.

central ionic-covalent Se1-Bi bond and the outermost van der Waals Se2-Se2 bond are the driving forces of ETT, whereas many high-pressure experiments of XRD, Raman, resistivity, and thermopower emphasized that the ETT in the layered 3D TIs materials is associated with the van der Waals forces [5]. The distant Se-Se ionic-covalent bonds inside a QL (Se1-Se1, Se1-Se2, and Se2-Se2) show a turning point at 7 GPa and then keep nearly constant at 7–10.4 GPa (red average line). All the measured Se-Bi/Se bonds decrease substantially at higher pressures (>10.4 GPa). Our results provide a more comprehensive picture on the intralayer ionic-covalent bands and interlayer van der Waals bonds in the QLs of Bi_2Se_3 upon compression.

It is believed that the ETT is induced by a topological change in the Fermi surface as the Brillouin zone is strongly deformed, which is difficult to explore experimentally [38]. In order to study the electronic states of the R-3m phase in terms of the obtained local structure, we optimized the precise Wyckoff positions of Bi (6c) and Se (6c) sites in the R-3m structure using the obtained values of Se2-Bi and Se1-Bi bonds. In the R-3m structure, the Bi and Se2 atoms occupy the 6c sites with 3m symmetry, whereas the Se1 atom is on the central (3a) site with $-3m$ symmetry. The cell dimension of the R-3m phase was measured by *in situ* XRD [e.g., Fig. 5(a)]. *In situ* XRD indicates that Bi_2Se_3 keeps the ambient rhombohedral structure (R-3m) at 11 GPa but

TABLE I. Parameters of linear fit $y = a + bx$ on the bond distances of Bi-Se1, Bi-Se2, and Se2-Se2 in the quintuple layer of Bi_2Se_3.

		Linear fit range (0–3 GPa)		Linear fit range (3–9.5 GPa)	
Bond	Bond type	a (Å)	b (Å/GPa)	a (Å)	b (Å/GPa)
Se1-Bi	Ionic-covalent	3.15626(680)	−0.04579(662)	3.10255(900)	−0.02596(142)
Se2-Bi	Ionic-covalent	2.84169(486)	−0.01061(483)	2.83965(616)	−0.00750(103)
Se2-Se2	van der Waals	3.38365(919)	−0.04090(873)	3.34267(667)	−0.02281(096)

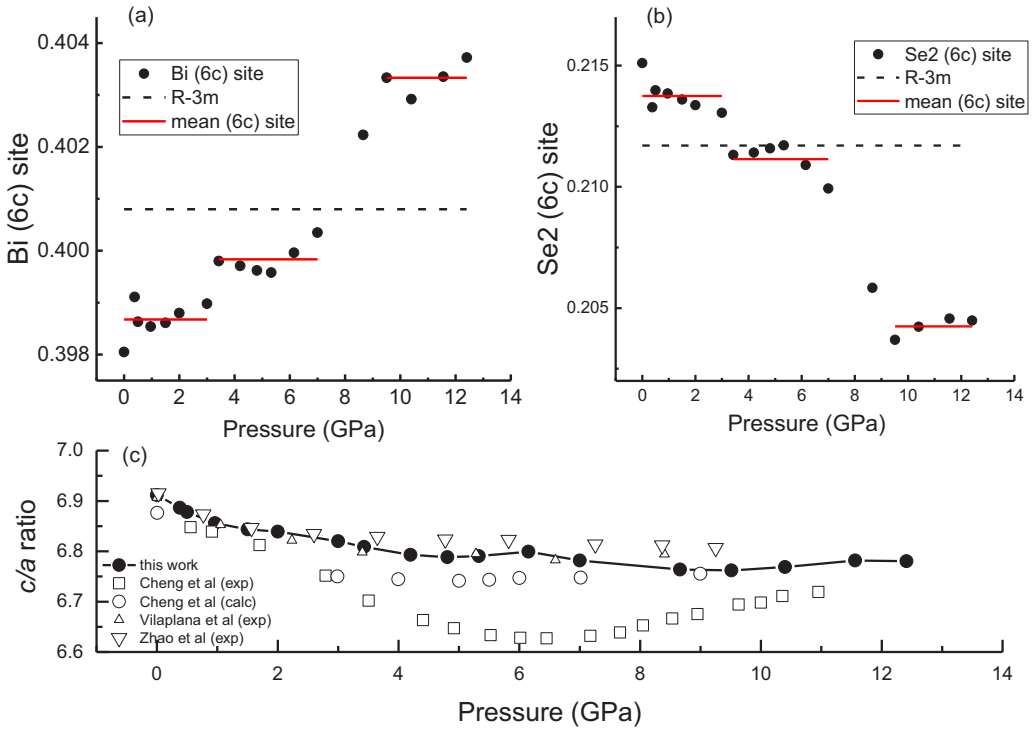

FIG. 7. The optimized *R*-3*m* structure based on the XAFS and XRD experiments: (a) Bi (6*c*) site and (b) Se2 (6*c*) sites. Red lines are the averaged values in the respective pressure ranges for clarification; (c) the obtained *c*/*a* ratio of the *R*-3*m* phase with previous data [4,17,36] for comparison.

mixed slightly with the emerging Bragg peaks of the $C2/m$ phase at 13 GPa (Fig. 2). We were then able to construct the experimental crystalline structural models (crystallographic information files) at high pressure for further DFT.

Figures 7(a) and 7(b) show the optimized Bi (6*c*) and Se2 (6*c*) sites from the combination of XAFS and XRD experiments. It is clear that both the Bi (6*c*) and the Se (6*c*) sites show a distinct stepwise pressure dependence. Red lines are the averaged values in the respective pressure range for clarification. This stepwise dependence indicates the existence of three distinct intermediate states in the isostructural *R*-3*m* phase at high pressure. Figure 7(c) shows the obtained *c*/*a* ratio of the *R*-3*m* phase, which agrees with previous data [4,17,36]. However, the values of the *c*/*a* ratio from different experiments are quite scattered, implying that the XRD-averaged structure may not be sufficient to characterize the structural features in details for the *R*-3*m* phase under pressure. So far, it is believed that the ETT is an IPT without modified Wyckoff positions of atoms and discontinuity in volume but with a pronounced change in the *c*/*a* ratio. It is known that the conventional powder XRD experiment suffers from difficulties in determining the precise Wyckoff positions of atoms in the crystal, leading to the XRD proof for the ETT remains controversial [5,14].

Figure 8 shows the calculated band structure of Bi_2Se_3 at high pressure including the spin-orbit interaction. The result at ambient pressure is coincident with the published band structures of Bi_2Se_3 [14,39]. As shown in Fig. 8(a), the band gap is gradually opened as the valence band moves to deeper and deeper levels as pressure increases, whereas little change in the conduction band. This change in the valence band suggests a pressure-induced carriers transition in Bi_2Se_3 from a *p*-type (hole-dominated) to a *n*-type (electron-dominated) semiconductor upon compression. This pressure-induced band-gap opening in Bi_2Se_3 has been experimentally observed in the Fourier-transform infrared (FTIR) optical experiment [15]. It is further proposed that the band-gap opening is helpful to trap the three-dimensional electrons and the two-dimensional (2D) carriers then become dominant in the 3D TI Bi_2Se_3 [15]. It is worth mentioning that the change in semiconductor carriers from *p* type to *n* type [Fig. 8(a)] has been observed experimentally in a similar TI material Bi_2Te_3, whose Hall coefficient changes from positive to negative during the transition, i.e., a crossover of the electron state from the *p* type to the *n* type in Bi_2Te_3 [6]. Also, *n*-type carriers have been observed in the $Cu_xBi_2Se_3$ superconductor [40]. It is clear that high pressure is a valuable tool to regulate the competition between 3D and 2D carriers, i.e., being helpful for understanding the ETT and topological superconductivity [5].

From the expanded region at the Γ point [Fig. 8(b)], we can find that the conduction band starts to indent at pressures above 3 GPa and finally splitting into two peaks at pressures above 6 GPa, i.e., the sign symbol reversed in the second-order derivative of the energy bands. Such a change in sign symbol can be directly testified by the Hall coefficient measurement [10], which is very sensitive to the changes in Fermi surface and electrical transportation [10,41]. It is believed that the ETT or the Lifshitz transition [38] is driven by the topological change in conduction-band extremum (Van Hove singularity).

Figure 9 shows the calculated direct and indirect band gaps of Bi_2Se_3, respectively, at the Γ point (a) and the smallest band gap (b) as a function of pressure together with the

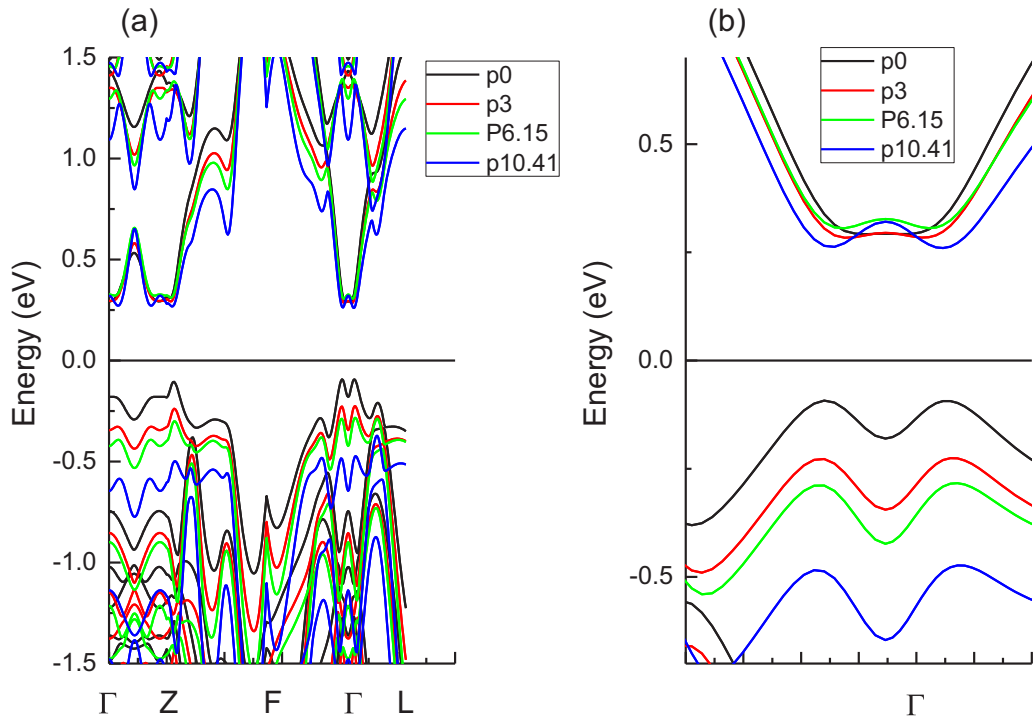

FIG. 8. (a) Calculated band structure of Bi_2Se_3 including spin-orbit interaction. Notation for high-symmetric points in the Brillouin zone is the same as in Ref. [11]. (b) Expanded region at the Γ point. We note that the conducting band starts indenting (>3 GPa) and finally splitting (>6 GPa) at the Γ point.

values of previous experimental and theoretical studies made by Segura *et al.* [15] and Bera *et al.* [14] for comparison. All the direct band gaps at the Γ point keep opening as pressure increases. Our calculated values are in good agreement with that of Bera *et al.* [14] at low pressures below 2 GPa but remain divergent with that of Segura *et al.* [15]. However, it

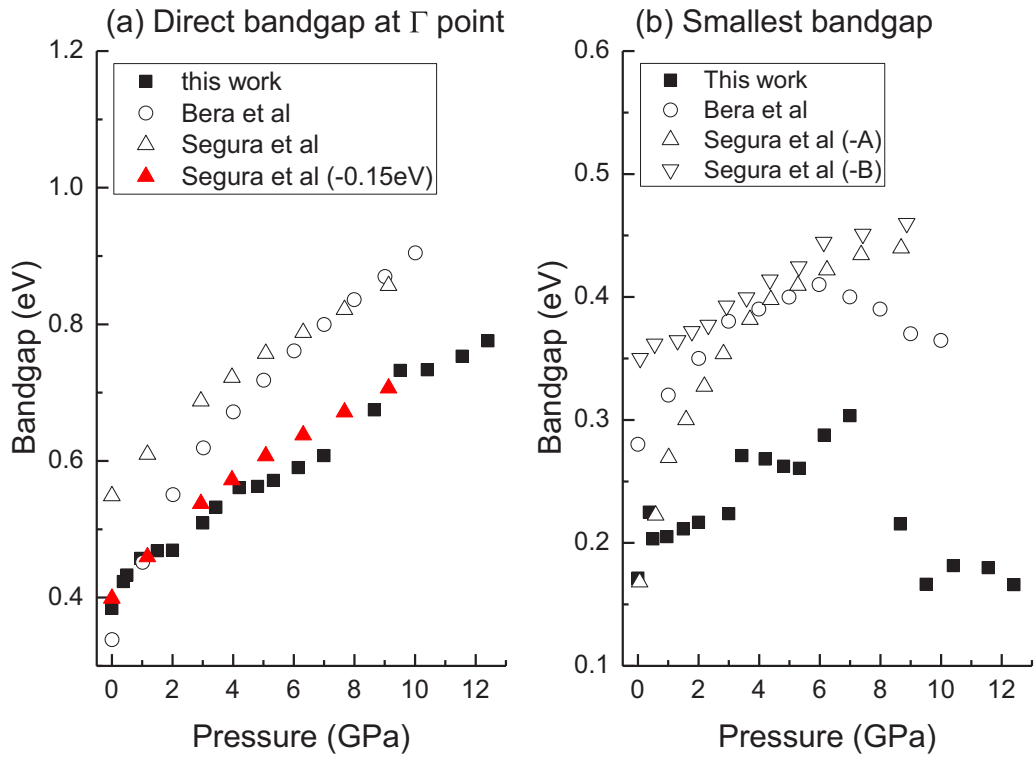

FIG. 9. Calculated band gap of Bi_2Se_3 as a function of pressure: (a) direct band gap at the Γ point and (b) the smallest band gap together with the values of previous studies by Segura *et al.* [15] and Bera *et al.* [14].

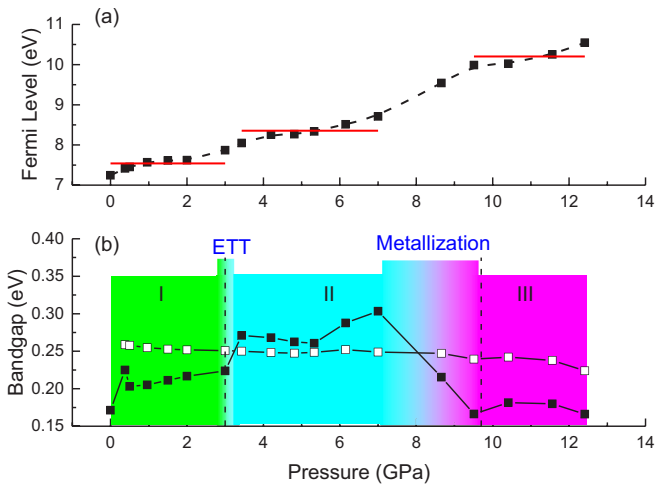

FIG. 10. Influence of atomic local structure on the *e* states of Bi_2Se_3 at high pressure: (a) Fermi levels; (b) Values of the band gap with (solid) and without (open) XAFS optimized local structure for comparison.

becomes well coincident over the entire pressure range with the shifted ones of Segura *et al.* [15] by an offset of −0.15 eV. It is known that the absolute values of the direct band gap at the Γ point depend considerably on the employed methods of the GGA approximation and spin-orbit interaction in the DFT calculations, which may result in a certain overestimation on the band-gap calculation [15]. For the indirect band gap [Fig. 9(b)], our calculated values agree well with the experimental optical observation of sample A at low pressures [15]. At higher pressures, the plateau at 3–7 GPa can be also roughly traced for the indirect band-gap data of Bera *et al.* [14].

Figure 10 shows the Fermi levels and band gaps of optimized Bi_2Se_3 structures at high pressure. The values of the Fermi levels show a positive dependence upon compression [Fig. 10(a)], i.e., a feature of a *n*-type (electron-dominated) semiconductor (Fig. 8). As clearly shown in Fig. 10(a), the Fermi level also exhibits a striking stepwise pressure dependence, confirming the existence of three distinct structural states observed in the local structure of the *R*-3*m* phase [Figs. 7(a) and 7(b)].

As shown in Fig. 10(b), there are two remarkable changes in the band gap of the *R*-3*m* phase, one narrow transition at ∼3 GPa, and other relatively broad transitions at 7–9.5 GPa. These abrupt changes in band gap are basically corresponding to the discontinuities of electrical transport properties in Bi_2Se_3, i.e., the pressure-induced ETT (2–4 GPa) and metallization (9.7 GPa) [10]. The overall increase in the band gap below 7 GPa is in accordance with the optical measurement [15] and previous calculation [14] [Fig. 9(b)]. The FTIR optical experiment indicates that the optical gap of Bi_2Se_3 increases from 0.17 eV at ambient pressure to 0.45 eV at 8 GPa [15]. This pressure-induced band-gap opening has been also observed by the recent electrical resistivity measurements, which suggests that the insulating state of Bi_2Se_3 becomes increasingly stable as pressure increases [10]. The closure of the indirect band gap at 7–9.5 GPa should reflect the gradual metallization of Bi_2Se_3 above 9.7 GPa [10].

It should be mentioned that there is a significant difference in the band gap between the XAFS optimized and unoptimized *R*-3*m* local structures [Fig. 10(b)]. The band gap of the unoptimized *R*-3*m* phase just keeps closing as pressure increases, which is not supported by the transport measurements [10,15]. Such a decisive difference illustrates the importance of an atomic local structure for a correct calculation on the electronic states of TI materials. Here, we can conclude that it is critically important to combine the XAFS optimized local structure with the long-range-order structure for exploring the novel physics in topological insulators under extreme conditions.

IV. CONCLUSION

To summarize, the combination of high-quality HP-XAFS using NPD anvils, XRD, and density functional theory calculation paves an effective way to probe the subtle changes in the local structure as well as the electronic states for the isostructural phase transition in TIs at high pressure. We have observed three pressure-induced distinct intermediate states in the rhombohedral phase of Bi_2Se_3. Our results indicate that local structure plays a critical role in the electronic states and the novel physics in the topological insulator Bi_2Se_3 under high pressure.

ACKNOWLEDGMENTS

We thank T. Lanzirotti, S. Tkachev, X. M. Yu, and N. Lazarz for their assistance with the experiments. HPSTAR is supported by the National Natural Science Foundation of China (Grant No. U1530402). The GSECARS sector of APS is supported by the NSF (Grant No. EAR-1128799) and the DOE (Grant No. DE-FG02-94ER14466). H.-K.M was supported by NSF Grants No. EAR-1345112 and No. EAR-1447438. Y.D. acknowledges support from National Key Research and Development Program of China Grant No. 2018YFA0305703, the Science Challenge Project, Grant No. TZ2016001, and The National Natural Science Foundation of China (NSFC) Grants No. U1930401 and No. 11874075.

[1] P. Janíček, Č. Drašar, L. Beneš, and P. Lošťák, Cryst. Res. Technol. **44**, 505 (2009).

[2] H. Zhang, C.-X. Liu, X.-L. Qi, X. Dai, Z. Fang, and S.-C. Zhang, Nat. Phys. **5**, 438 (2009).

[3] Y. Zhang, K. He, C.-Z. Chang, C.-L. Song, L.-L. Wang, X. Chen, J.-F. Jia, Z. Fang, X. Dai, W.-Y. Shan *et al.*, Nat. Phys. **6**, 584 (2010).

[4] R. Vilaplana, D. Santamaría-Pérez, O. Gomis, F. J. Manjón, J. González, A. Segura, A. Muñoz, P. Rodríguez-Hernández, E. Pérez-González, V. Marín-Borrás *et al.*, Phys. Rev. B **84**, 184110 (2011).

[5] F. J. Manjón, R. Vilaplana, O. Gomis, E. Pérez-González, D. Santamaría-Pérez, V. Marín-Borrás, A. Segura, J. González, P. Rodríguez-Hernández, A. Muñoz *et al.*, Phys. Status Solidi B **250**, 669 (2013).

[6] J. L. Zhang, S. J. Zhang, H. M. Weng, W. Zhang, L. X. Yang, Q. Q. Liu, S. M. Feng, X. C. Wang, R. C. Yu, L. Z. Cao *et al.*, Proc. Natl. Acad. Sci. USA **108**, 24 (2011).

[7] J. Zhu, J. L. Zhang, P. P. Kong, S. J. Zhang, X. H. Yu, J. L. Zhu, Q. Q. Liu, X. Li, R. C. Yu, R. Ahuja *et al.*, Sci. Rep. **3**, 2016 (2013).

[8] E. S. Itskevich, L. M. Kashirskaya, and V. F. Kraidenov, Semiconductors **31**, 276 (1997).

[9] N. V. Chandra Shekar, D. A. Polvani, J. F. Meng, and J. V. Badding, Physica B **358**, 14 (2005).

[10] J. Zhang, Y. Han, C. Liu, X. Zhang, F. Ke, G. Peng, Y. Ma, Y. Ma, and C. Gao, Appl. Phys. Lett. **105**, 062102 (2014).

[11] X.-L. Qi, T. L. Hughes, S. Raghu, and S.-C. Zhang, Phys. Rev. Lett. **102**, 187001 (2009).

[12] X.-L. Qi and S.-C. Zhang, Rev. Mod. Phys. **83**, 1057 (2011).

[13] G. K. Pradhan, A. Bera, P. Kumar, D. V. S. Muthu, and A. K. Sood, Solid State Commun. **152**, 284 (2012).

[14] A. Bera, P. Koushik, D. V. S. Muthu, U. V. Waghmare, and A. K. Sood, J. Phys.: Condens. Matter **28**, 105401 (2016).

[15] A. Segura, V. Panchal, J. F. Sánchez-Royo, V. Marín-Borrás, V. Muñoz-Sanjosé, P. Rodríguez-Hernández, A. Muñoz, E. Pérez-González, F. J. Manjón, and J. González, Phys. Rev. B **85**, 195139 (2012).

[16] N. P. Butch, K. Kirshenbaum, P. Syers, A. B. Sushkov, G. S. Jenkins, H. D. Drew, and J. Paglione, Phys. Rev. B **81**, 241301(R) (2010).

[17] Z. Jinggeng, L. Haozhe, E. Lars, D. Dawei, C. Zhiqiang, and G. Genda, J. Phys.: Condens. Matter **25**, 125602 (2013).

[18] Z. Yu, L. Wang, Q. Hu, J. Zhao, S. Yan, K. Yang, S. Sinogeikin, G. Gu, and H.-k. Mao, Sci. Rep. **5**, 15939 (2015).

[19] G. Liu, L. Zhu, Y. Ma, C. Lin, J. Liu, and Y. Ma, J. Phys. Chem. C **117**, 10045 (2013).

[20] H.-K. Mao, X.-J. Chen, Y. Ding, B. Li, and L. Wang, Rev. Mod. Phys. **90**, 015007 (2018).

[21] C. Zhang, L. Sun, Z. Chen, X. Zhou, Q. Wu, W. Yi, J. Guo, X. Dong, and Z. Zhao, Phys. Rev. B **83**, 140504(R) (2011).

[22] K. Kirshenbaum, P. S. Syers, A. P. Hope, N. P. Butch, J. R. Jeffries, S. T. Weir, J. J. Hamlin, M. B. Maple, Y. K. Vohra, and J. Paglione, Phys. Rev. Lett. **111**, 087001 (2013).

[23] G. Shen and H. K. Mao, Rep. Prog. Phys. **80**, 016101 (2016).

[24] H. Zhu, J. Dong, P. Li, Y. Wang, Z. Guo, X. Shan, Y. Gong, P. An, X. Li, J. Zhang *et al.*, Phys. Status Solidi B **254**, 1700007 (2017).

[25] X. Hong, M. Newville, V. B. Prakapenka, M. L. Rivers, and S. R. Sutton, Rev. Sci. Instrum. **80**, 073908 (2009).

[26] T. Irifune, A. Kurio, S. Sakamoto, T. Inoue, and H. Sumiya, Nature (London) **421**, 599 (2003).

[27] N. Ishimatsu, K. Matsumoto, H. Maruyama, N. Kawamura, M. Mizumaki, H. Sumiya, and T. Irifune, J. Synchrotron Radiat. **19**, 768 (2012).

[28] B. Ravel and M. Newville, J. Synchrotron Radiat. **12**, 537 (2005).

[29] M. Newville, J. Synchrotron Radiat. **8**, 96 (2001).

[30] A. P. Hammersley, S. O. Svensson, M. Hanfland, A. N. Fitch, and D. Hausermann, High Pressure Res. **14**, 235 (1996).

[31] V. Petříček, M. Dušek, and L. Palatinus, Z. Kristallogr. - Cryst. Mater. **229**, 345 (2014).

[32] J. P. Perdew and A. Zunger, Phys. Rev. B **23**, 5048 (1981).

[33] X. Hua, X. Chen, and W. A. Goddard, Phys. Rev. B **55**, 16103 (1997).

[34] G. Paolo, B. Stefano, B. Nicola, C. Matteo, C. Roberto, C. Carlo, C. Davide, L. C. Guido, C. Matteo, D. Ismaila *et al.*, J. Phys.: Condens. Matter **21**, 395502 (2009).

[35] J. P. Perdew, K. Burke, and M. Ernzerhof, Phys. Rev. Lett. **77**, 3865 (1996).

[36] H. Cheng, J. Zhang, Y. Li, G. Li, and X. Li, J. Appl. Phys. **121**, 225902 (2017).

[37] B. Wölfing, C. Kloc, J. Teubner, and E. Bucher, Phys. Rev. Lett. **86**, 4350 (2001).

[38] I. M. Lifshitz, Sov. Phys. JETP **11**, 1130 (1960).

[39] S. M. Young, S. Chowdhury, E. J. Walter, E. J. Mele, C. L. Kane, and A. M. Rappe, Phys. Rev. B **84**, 085106 (2011).

[40] Y. S. Hor, A. J. Williams, J. G. Checkelsky, P. Roushan, J. Seo, Q. Xu, H. W. Zandbergen, A. Yazdani, N. P. Ong, and R. J. Cava, Phys. Rev. Lett. **104**, 057001 (2010).

[41] A. Hackl and M. Vojta, Phys. Rev. Lett. **106**, 137002 (2011).